

Foams generated from viscous non-Newtonian shear-thinning liquids in a continuous multi rotor-stator device

Jabarkhyl, Saifullah; Barigou, Mostafa; Zhu, Shiping; Rayment, Pip; Lloyd, David M.; Rossetti, Damiano

DOI:

[10.1016/j.ifset.2019.102231](https://doi.org/10.1016/j.ifset.2019.102231)

License:

Creative Commons: Attribution-NonCommercial-NoDerivs (CC BY-NC-ND)

Document Version

Peer reviewed version

Citation for published version (Harvard):

Jabarkhyl, S, Barigou, M, Zhu, S, Rayment, P, Lloyd, DM & Rossetti, D 2020, 'Foams generated from viscous non-Newtonian shear-thinning liquids in a continuous multi rotor-stator device', *Innovative Food Science and Emerging Technologies*, vol. 59, 102231. <https://doi.org/10.1016/j.ifset.2019.102231>

[Link to publication on Research at Birmingham portal](#)

General rights

Unless a licence is specified above, all rights (including copyright and moral rights) in this document are retained by the authors and/or the copyright holders. The express permission of the copyright holder must be obtained for any use of this material other than for purposes permitted by law.

- Users may freely distribute the URL that is used to identify this publication.
- Users may download and/or print one copy of the publication from the University of Birmingham research portal for the purpose of private study or non-commercial research.
- User may use extracts from the document in line with the concept of 'fair dealing' under the Copyright, Designs and Patents Act 1988 (?)
- Users may not further distribute the material nor use it for the purposes of commercial gain.

Where a licence is displayed above, please note the terms and conditions of the licence govern your use of this document.

When citing, please reference the published version.

Take down policy

While the University of Birmingham exercises care and attention in making items available there are rare occasions when an item has been uploaded in error or has been deemed to be commercially or otherwise sensitive.

If you believe that this is the case for this document, please contact UBIRA@lists.bham.ac.uk providing details and we will remove access to the work immediately and investigate.

1 **Foams generated from viscous non-Newtonian shear-thinning liquids**
2 **in a continuous multi rotor-stator device**
3
4
5
6

7 **Saifullah Jabarkhyl¹, Mostafa Barigou^{1*}**

8 **Shiping Zhu², Pip Rayment², David M. Lloyd², Damiano Rossetti²**

9 ¹School of Chemical Engineering, University of Birmingham, Edgbaston, Birmingham B15 2TT, UK

10 ²Unilever R&D Refreshment Discovery, Colworth Science Park, Sharnbrook, MK44 1LQ, UK
11
12
13
14
15
16
17

18 **Abstract**

19 Whilst aeration is ubiquitous in the food industry, little work has been done on foams generated from
20 viscous non-Newtonian liquids. We study the production of foams from viscous shear-thinning
21 liquids containing a non-ionic food grade surfactant (PGE 55), Xanthan gum and caster sugar, using a
22 continuous pilot-scale device having twelve rotor-stator pairs. The effects of process parameters
23 (rotor speed, gas-liquid volumetric flowrate ratio (G/L)) and liquid composition (surfactant
24 concentration, Xanthan gum concentration) on foam gas volume fraction and bubble size distribution
25 are elucidated. X-ray micro-Computed Tomography is employed to characterise the 3D
26 microstructure of the foams. Rotor speed and G/L ratio are the dominant factors in determining the
27 gas volume fraction and bubble size distribution. The foams produced exhibit a rich fine texture with
28 high static stability. For a given energy input, a higher G/L ratio results in a higher gas fraction and a
29 smaller bubble size.
30

31 **Keywords:** Continuous foaming; non-Newtonian liquid; X-ray micro-CT; Rheology; Bubble size
32 distribution.
33
34
35
36
37
38
39
40

41 *Corresponding author: m.barigou@bham.ac.uk

42 1. Introduction

43 Over the last 30 years, aerated food products have become increasingly popular since the inclusion of
44 air bubbles gives rise to a variety of microstructures which exhibit better textural and sensorial
45 properties (Campbell & Mougeot, 1999; Guo et al., 2017; Indrawati & Narsimhan, 2008).
46 Depending on the gas volume fraction (ϕ), aerated food products can be classified as wet foam (\sim
47 $0.50 > \phi < 0.95$) or dry foam ($\sim \phi > 0.95$). A foam consists of a continuous liquid phase in the form of a
48 network of thin lamellae and a dispersed gas phase in the form of bubbles ranging from microns to
49 millimetres in size (Bikerman, 1973; Walstra, 1989). Foams are thermodynamically unstable
50 structured fluids (Curschellas et al., 2012a; Corina Curschellas et al., 2012b; Germain & Aguilera,
51 2014). They are subject to three distinct destabilisation mechanisms: liquid drainage, bubble
52 coalescence and disproportionation (Cox, Aldred, & Russell, 2009; Kroezen & Wassink, 1987).

53
54 In the production of aerated products such as whipped cream, ice cream or mousse, it is important to
55 achieve a good degree of control of the air volume fraction and bubble size distribution since the
56 stability and the organoleptic properties of the product (creaminess, texture, mouthfeel) are strongly
57 dependent on these critical parameters. For example, small bubbles and uniform bubble size
58 distribution impart excellent foam stability and creaminess (Müller-Fischer, Suppiger, & Windhab,
59 2007b; Müller-Fischer & Windhab, 2005). Many techniques have been proposed for measuring
60 bubble size distribution including conductivity probes, optical fibre technique, light microscopy,
61 freezing and visualising foam cross-sections, X-ray micro-computed tomography (X-ray micro-CT),
62 ultrasonic reflectance spectroscopy and confocal scanning laser microscopy (Jang, Nikolov, Wasan,
63 Chen, & Campbell, 2005; Kulmyrzaev, Cancelliere, & McClements, 2000; Lim & Barigou, 2004).
64 Each of these methods has its own advantages and drawbacks. For example, light microscopy which
65 is commonly used is usually intrusive as it often requires sampling the foam and sometimes diluting
66 the sample especially when the bubble size is small and the bubble density is high. Other techniques
67 suffer from similar limitations which involve significant tampering with the foam samples. By
68 contrast, however, X-ray micro-CT is a non-destructive and non-intrusive technique and can be
69 utilised to image stable foams to reveal their full 3D microstructure with a high degree of accuracy
70 (Lim & Barigou, 2004).

71
72 Food foams are generated using a number of different techniques including mechanical whipping,
73 membrane foaming, gas sparging (Pugh, 2016). At pilot and industrial scales, mechanical whipping
74 devices are preferred as they are more amenable to continuous large-scale production and better
75 process control. In this respect, continuous rotor-stator devices are popular especially when
76 processing viscous and non-Newtonian liquids (Hanselmann & Windhab, 1998; Kroezen, Groot
77 Wassink, & Bertlein, 1988; Kroezen & Wassink, 1987; Mary et al., 2013; Mezdour, Séguineau de
78 Préval, Granda, Cuvelier, & Ducept, 2017; Müller-Fischer et al., 2007b; Narchi, Vial, Labbafi, &

79 Djelveh, 2011; Nicorescu et al., 2010). The first study using a continuous rotor-stator device was by
80 Krozen and Wassink (1988). Smaller bubbles were obtained at higher rotational speeds and lower air
81 volume fractions. In addition, air inclusion was found to be good in the turbulent flow regime, poor in
82 transitional flow and moderate in laminar flow. A number of studies then followed which studied the
83 effects of liquid mix properties (density, viscosity and surface tension) and processing parameters
84 (rotor speed, air volume fraction, power input, residence time, static pressure and temperature in the
85 mixing-head chamber). For example, using a single non-Newtonian fluid and a fixed twelve rotor-
86 stator geometry operating at a single speed, Muller-Fischer and Windhab (2005) found that bubble
87 size increased as the gas-liquid ratio inside the mixing-head chamber was increased ($G/L = 0.5-3.5$)
88 covering laminar to transitional flow, and this was attributed to bubble coalescence. Nicorescu et al.
89 (2010), on the other hand, using a fixed seven rotor-stator geometry, a fixed non-Newtonian fluid and
90 a single G/L ratio of 2.0, investigated the effects of rotor speed and residence time on aeration
91 efficiency and bubble size. Rotor speed was found to be the main processing parameter affecting
92 bubble size, but no reference was made to the flow regime and how it influences bubble size and
93 aeration efficiency. Narchi et al. (2011) also investigated the effects of rotor speed on bubble size for
94 a fixed Newtonian and a fixed non-Newtonian medium under laminar conditions. For both fluid
95 systems, bubble size was found to decrease with rotor speed. For the Newtonian fluid, bubble size
96 also decreased as a function of G/L ratio but no explanation was given. This effect was not
97 investigated for the non-Newtonian system.

98

99 No systematic studies have hitherto been reported on the combined effects of liquid composition
100 (surfactant concentration, thickener concentration) and processing parameters (rotor speed, G/L ratio)
101 for non-Newtonian media which are most relevant to the production of food foams. Furthermore, the
102 vast majority of the literature on continuous foaming has considered model food foams stabilized by
103 proteins, with non-ionic surfactants receiving much less attention. Apart from their different
104 absorption kinetics, the mechanisms of bubble stabilization by the latter surface active agents are also
105 different. In this paper, we present the first extensive study of wet foams generated from viscous non-
106 Newtonian shear-thinning liquids using a continuous multi rotor-stator device and a non-ionic
107 surfactant. A range of experimental conditions are investigated to determine the effects of liquid
108 formulation and processing conditions on foam bubble size distribution, gas volume fraction and
109 static stability. Foaming is carried out under atmospheric conditions to avoid foam expansion which
110 can bring about drastic changes in foam microstructure which is uncontrollable and undesirable
111 (Müller-Fischer et al., 2007b). We use an advanced X-ray micro-CT technique to non-invasively
112 visualise and analyse the 3D microstructure of the foams.

113

114 2. Materials and methods

115 2.1 Model fluids preparation and characterisation

116 The model fluids employed in the experiments consisted of a mixture of polyglycerol fatty acid ester
117 (PGE 55, DuPont, Denmark), Xanthan gum (XG, supplied by Unilever), caster sugar (British sugar
118 PLC, obtained from local supermarket) and sodium azide (ReagentPlus, $\geq 99.5\%$, Sigma Aldrich),
119 used without prior purification. A Silverson high-shear mixer (Model L4RT, Silverson, UK) was
120 used to mix the ingredients in distilled water held at 80°C using a water bath, to ensure that the
121 Krafft temperature (58°C) of PGE 55 was exceeded (Curschellas et al., 2012a; Duerr-Auster, Eisele,
122 Wepf, Gunde, & Windhab, 2008). First, polyglycerol fatty acid ester (PGE 55) was added under
123 agitation (6000-7000 rpm) and mixed thoroughly for at least 5 minutes prior to adding sugar and XG.
124 Stirring was continued for another 5 min until all XG was completely dissolved. Sodium azide (0.025
125 wt%) was added to prevent microbial growth. The model fluids were then stored at room temperature
126 to degass and mature (hydration of XG) for at least 24 hours, to enable their rheology to fully
127 stabilise. In order to check that the high-shear processing used did not affect the rheology of the
128 fluids, we also prepared smaller volumes of such liquids using gentle mixing provided by a magnetic
129 stirrer. There was no significant difference between the liquids obtained.

130
131 The equilibrium surface tension of the fluids was measured at 25°C using a Wilhelmy plate method
132 (Sigma 701 Force Tensiometer). Dynamic surface tension measurements were obtained using a
133 pendant drop method (PAT1P Tensiometer, Sinterface, Germany). Prior to any measurement,
134 solutions were centrifuged for 4 minutes at a rotational speed of 2800 rpm to remove entrapped air
135 bubbles. Each measurement was repeated at least three times and an average taken ($SD = 1.5 \text{ mN m}^{-1}$).
136

137
138 Table 1 summarises the composition of the model fluids and their physical properties; the density of
139 all fluids was equal to 1080 kg m^{-3} . The presence of caster sugar and XG, had negligible effects on
140 the surface tension as the surface activity of PGE 55 is much greater than both caster sugar and XG.
141 For all model fluids tested, surface tension was shown to evolve with respect to time, with a rapid
142 initial reduction followed on by a gradual decline tending towards an equilibrium value. Equilibrium
143 values of surface tension are given in Table 1. As shown and expected, surface tension kinetics was
144 found to be a function of PGE 55 and XG concentration.

145
146 A controlled stress/strain rheometer (Discovery HR-2, Hybrid Rheometer, TA, USA) equipped with a
147 40 mm parallel plates geometry was used to characterise the rheology of the model fluids. No slip
148 was detected and measurements conducted using different plate gaps (and alternatively a cone-and-
149 plate geometry) yielded the same results. Complete flow curves were obtained at controlled strain
150 rate by varying the shear rate in the range of $0.001\text{--}8000 \text{ s}^{-1}$, and were well fitted by the Cross
151 rheological model (coefficient of determination, $R^2 \sim 0.999$). The cross model incorporates both the

152 upper and limiting viscosities, η_o and η_∞ , corresponding, respectively, to the upper and lower
153 Newtonian regions, and is given by:

154

$$155 \quad \eta = \eta_\infty + \frac{\eta_o - \eta_\infty}{1 + (c\dot{\gamma})^m} \quad (1)$$

156

157 where η is the apparent viscosity, $\dot{\gamma}$ is the shear rate, and c and m are the Cross time constant and rate
158 constant, respectively. This model can be reduced to the power law model in the region where $\eta \ll \eta_o$
159 and $\eta \gg \eta_\infty$, which will be useful for the definition of a modified Weber number, as discussed further
160 below.

161

162 **2.2 Foam generation**

163 A pilot-scale continuous rotor-stator (Megatron FM 12- 50/2 HR), shown in Fig. 1, was used to aerate
164 the model fluids and continuously generate foam. The device consists of 12 rotor-stator pairs in series
165 where the rotor and stator have diameters of 50 and 43 mm each. Every rotor and stator has 13 pins
166 (4.7 x 4.6 x 2.5 mm) with square ends and the gap between the rotor and stator is 1.0 mm. The
167 geometrical dimensions of the rotor-stator pairs are provided in Table 2.

168

169 A progressive cavity pump is utilised to continuously pump the liquid at a controlled flowrate to the
170 mixing-head chamber which has a free volume of approximately 85 mL. Simultaneously, a controlled
171 amount of air is also introduced into the feed line from a gas cylinder, which combines with the liquid
172 upon entering the mixing-head chamber. Foam was generated at atmospheric pressure using rotor
173 speeds in the range 500-1750 rpm. A Julabo F-25 cooler (JULABO GmbH, Germany) was used to
174 dissipate the heat generated during operation and control the mixing-head temperature, so that the exit
175 foam temperature was maintained approximately equal to the liquid feed temperature at $20 \pm 3^\circ\text{C}$,
176 which kept the effects on fluid rheology and surfactant kinetics minimal.

177

178 Experiments were conducted to generate foams with varying microstructure by using combinations of
179 liquid flowrate values within the range $3.46 - 6.67 \text{ Lh}^{-1}$ and air flowrate values within the range $5.0 -$
180 10.1 Lhr^{-1} . These experiments showed a high degree of reproducibility in terms of foam gas volume
181 fraction and mean bubble size, i.e. within 5% at the lowest rotor speed and within 1% at the highest
182 speed.

183

184 **2.3 Foam characterisation**

185 **2.3.1 Air volume fraction**

186 The air volume fraction in the foam is theoretically defined as:

187

$$188 \quad \phi_{th} = \frac{Q_G}{Q_G + Q_L} \quad (2)$$

189 where Q_G and Q_L are, respectively, the air and liquid volumetric flowrate. This was experimentally
190 measured by collecting foam samples at the exit of the rotor-stator device and determining the average
191 mass of base liquid and foam that fill the same volume. The experimentally measured ϕ_e value cannot
192 be greater than the theoretical value (ϕ_{th}). An efficient foaming process will aim to maximise ϕ_e .
193

194

195 2.3.2 *Bubble size distribution*

196 Two techniques were utilised to obtain the foam bubble size distribution. The first technique is a
197 well-established method which uses a light microscope (ZEISS, Axiovert 200M) and a digital camera.
198 Foam samples were diluted using the base liquid and then carefully transferred to a viewing chamber
199 according to the protocol described by Gaillard et al. (2017). A minimum of 500 bubbles were
200 measured in each sample to avoid statistical bias, using ImageJ software
201 (<https://imagej.nih.gov/ij/index.html>). The second method used a desktop X-ray micro-CT (Skyscan
202 1172, Bruker, Belgium) to scan and visualise, non-invasively, the full 3D microstructure of the foam
203 samples (3.8 μm resolution). A 2-5 mL foam sample was placed inside a drinking straw and sealed
204 prior to scanning (Barigou & Douaire, 2013; Lim & Barigou, 2004). From the bubble size
205 distribution, the Sauter mean bubble diameter was obtained:

206

$$207 \quad D_{32} = \frac{\sum n_i d_i^3}{\sum n_i d_i^2} \quad (3)$$

208 where n is the number of bubbles of diameter d in class size i .

209

210 2.3.3 *Foam stability*

211 Foam stability is determined by liquid drainage, bubble coalescence and Ostwald ripening. Foam
212 drainage was measured over a period of many weeks by monitoring a 50 mL foam sample collected at
213 the outlet of the continuous rotor-stator and stored at a constant temperature of 25°C. Thus, transients
214 of drained liquid were obtained for all experimental conditions investigated. Foam collapse was
215 measured by monitoring the height of standing foams. Foam coarsening which is a consequence of
216 bubble coalescence and Ostwald ripening was investigated using X-ray micro-CT, by scanning foam
217 samples also stored at constant temperature (25°C) on a weekly basis over a period of several weeks.

218

219 2.3.4 *Foam rheology*

220 Foam rheometry was conducted at 25°C using the stress/strain controlled rheometer and parallel-plate
221 geometry described above. In this case, minor slip was observed but this was eliminated by using
222 roughened plates (58 μm equivalent grit size). The parallel-plate gap was fixed at 2 mm which is
223 approximately an order of magnitude larger than the largest bubble size. Complete flow curves were
224 obtained at controlled strain rate by varying the shear rate in the range of 0.0001–1000 s^{-1} , and were
225 well fitted by the Cross model (coefficient of determination, $R^2 \sim 0.999$) defined in Eq. (1).

226

227 **2.4 Theory**

228 *2.4.1 Foam hydrodynamics inside mixing-head chamber*

229 The Hydrodynamics inside the mixing-head chamber play a crucial role in the production of
230 homogenous foams. The pertinent parameters are the Power number and the Reynolds number. The

231 Power number is the dimensionless form of the power input (P):

232

$$233 P_o = P/\rho_f N^3 D^5 \quad (4)$$

234 where N is the rotor speed and ρ_f is the density of the gas-liquid dispersion. The Power number is in
235 turn dependent on the value of Reynolds number (Re) defined as follows:

236

$$237 P_o = f(Re) \quad (5)$$

238

239 where Re is given by:

240

$$241 Re = \rho_f N D^2 / \eta(\dot{\gamma}) \quad (6)$$

242

243 where $\eta(\dot{\gamma})$ is the apparent foam viscosity at shear rate $\dot{\gamma}$.

244

245 Krozen and Wassink (1988) were the first to derive via an extensive study the empirical relationship
246 $P_o = f(Re)$ for a continuous rotor-stator device, by experimenting with different geometries and a
247 wide range of water-glycerol mixtures. Such a relationship was based on a generalised Power
248 number:

249

$$250 P_o^* = P_Z / \rho_F D^4 N^3 h L q \quad (7)$$

251

252 and a generalised Reynolds number :

253

$$254 Re^* = \rho_F N D s / (f \times \eta(\dot{\gamma})) \quad (8)$$

255

256 both of which are independent of rotor-stator device geometry. The correlation factor f in Eq. (8) is
257 defined as:

258

$$259 f = 710/q + 553s/\sqrt{Dq} \quad (9)$$

260

261 and the geometrical dimensions h , L , q , o and s are defined in Table 2. In the laminar flow regime
 262 ($Re^* < 0.01$), the Power number was found to be inversely proportional to the Reynolds number,
 263 whereas in the turbulent regime ($Re^* > 0.1$), P_o^* was found to be constant (equal to 17).

264

265 2.4.2 Energy dissipation inside mixing-head chamber

266 The energy consumption in our foaming experiments was estimated using the above empirical
 267 relationship $P_o = f(Re)$ developed by Krozen and Wassink (1988). This initially involved the
 268 identification of the flow regime using the definition of Re^* (Eq. (8)) and f (Eq. (9)), the dimensions
 269 of the rotor-stator geometry (Table 2) and the function $\mu(\dot{\gamma})$. For all experimental conditions
 270 investigated, Re^* was found to be in the range of 0.02–5.7, i.e. corresponding in the vast majority to
 271 turbulent flow where, as indicated above, P_o^* is constant and equal to 17.

272

273 The net mechanical power input per unit volume (P_v) is defined as:

274

$$275 P_v = \frac{P}{V} \quad (10)$$

276

277 where V is the volume of the mixing-head chamber (85 mL). The shear rate ($\dot{\gamma}$) inside the mixing-
 278 head chamber is the maximum shear rate at the tip of the rotor (Müller-Fischer, Bleuler, & Windhab,
 279 2007a):

280

$$281 \dot{\gamma} = \frac{\pi DN}{s} \quad (11)$$

282

283 The viscosity function of the foam $\eta(\dot{\gamma})$ is obtained by determining the rheological flow curve of
 284 foam samples taken at the outlet of the rotor-stator device using the rheometer described above.
 285 Finally, the net volumetric energy input (E_V) can be determined, thus:

286

$$287 E_V = \tau P_v \quad (12)$$

288

289 where τ is the average residence time of both the gas and liquid in the mixing-head chamber, given
 290 by:

291

$$292 \tau = \frac{V}{V_{foam}} = \frac{V}{Q_L + Q_G} \quad (13)$$

293

294 where V_{foam} is the volumetric flowrate of foam and Q_L and Q_G are the liquid and air volumetric
 295 flowrate, respectively.

296

297 **3 Results and discussion**

298 **3.1 Aeration efficiency**

299 Aeration efficiency is an important feature of the foam generation process which indicates the ability
300 to incorporate all of the available gas into the foaming liquid to make a homogeneous foam. Thus,
301 optimum aeration is achieved when the theoretical and experimental values of volume gas fraction (ϕ)
302 are equal (Eq. (2)). We studied the effects on the incorporated gas volume fraction of the processing
303 parameters (rotor speed, air and liquid volumetric flowrates) and the physical properties of the liquid
304 (dynamic surface tension, liquid viscosity). In the first set of experiments, the liquid flowrate was set
305 to 5 L hr⁻¹ and the air flowrate was varied between 5, 7.5 and 10.0 L hr⁻¹ to achieve foams with ϕ_{th}
306 values in the range of 0.50-0.67. When the G/L ratio was set to 1.0, all model fluids were able to
307 achieve maximum aeration, i.e. $\phi_e = \phi_{th}$, over the range of rotational speed 500-1750 rpm,
308 independent of the residence time (τ) and the composition of the liquid used, as shown in Table 3.

309

310 However, when the G/L ratio was increased to 1.5, a ‘blow-by’ phenomenon was observed for MF1 at
311 rotational speeds of 500 and 750 rpm and this was also independent of τ . The term ‘blow-by’ was
312 initially coined by Kroezen and Wassink (1988) who observed a large pocket of undispersed gas (slug
313 flow regime) at the outlet of the continuous rotor-stator, which is undesirable. The moderate
314 concentration of PGE 55 (0.2 wt%) seems to limit the incorporation of air in liquid MF1 at these
315 particular rotational speeds. This phenomenon may be attributed to bubble coalescence inside the
316 mixing-head chamber due to insufficient surfactant, as previously observed in turbulent emulsification
317 (Tcholakova et al., 2011). As G/L was increased, ‘blow-by’ occurred at higher and higher rotational
318 speeds and no homogeneous foam could be produced at any speed within the range studied when G/L
319 ≥ 2.5 . Fluids MF2 and MF3, with a higher PGE 55 content (0.5 wt% and 1 wt%, respectively), were
320 in fact able to achieve maximum air volume fraction at all rotational speeds investigated when G/L =
321 1.5. ‘Blow-by’ was observed, however, for both fluids regardless of residence time when G/L = 2.0 at
322 rotational speeds of 500 and 750 rpm, and at G/L = 2.5 it occurred at all rotational speeds. Thus, a
323 doubling in PGE 55 concentration between MF2 and MF3 had no influence on the onset of ‘blow-by’.
324 Fluids M4 and M5 have the same surfactant concentration as fluid MF2 but a lower Xanthan gum
325 concentration (Table 1); they exhibit ‘blow-by’ under the same conditions as MF2 but their foam
326 stability, bubble size distribution and rheological properties are significantly different. These results
327 seem to suggest that beyond a certain concentration, the aeration process is no longer determined by
328 surfactant content or the hydrodynamics of the process.

329

330 **3.2 Comparison between light microscopy and X-ray micro-CT**

331 Typical foam images produced from light microscopy and X-ray micro-Computed Tomography,
332 described above, are shown in Fig. 2. The corresponding Sauter mean bubble diameter (D_{32}) data are
333 plotted in Fig. 3 for G/L = 1 and 1.5. As shown, there are significant discrepancies between the two
334 sets of results. Light microscopy is a 2D technique which suffers from a number of shortcomings

335 including: (i) out-of-focus bubbles have to be manually detected and removed; any out-of-focus
336 bubbles not filtered out may introduce errors; (ii) bubbles larger than the gap of the viewing cell are
337 distorted, thus, giving rise to errors; and (iii) the size of bubble sample analysed (~ 500 - 1000) is
338 limited by the slow and tedious semi-automatic image processing. In comparison, X-ray micro-CT is
339 a non-invasive technique which yields the full 3D structure of the foam which can then be sliced and
340 examined along any plane. The number of 3D bubbles analysed in X-ray micro-CT is much greater
341 (~ 5000 - 15000) and the analysis is fully automated. In conclusion, the 3D X-ray micro-CT technique
342 is a more accurate and reliable technique and was adopted for the characterisation of the foams in this
343 study. More details on the advantages of X-ray micro-CT can be found in Barigou and Douaire
344 (2013).

345

346 **3.3 Effects of processing parameters and physical properties of foaming solution on bubble size**

347 *3.3.1 Effects of G/L ratio and residence time*

348 The effects of varying the rotor speed on the Sauter mean bubble diameter of the foam are shown in
349 Fig. 4 for fluids MF1, MF2 and MF3 at different G/L ratios. Irrespective of the model fluid and G/L
350 ratio, increasing N leads to a sharp reduction in bubble size as widely reported in the literature where
351 similar rotor-stator devices were used (Balerin, Aymard, Ducept, Vaslin, & Cuvelier, 2007; Mary et
352 al., 2013; Müller-Fischer et al., 2007b; Narchi et al., 2011; Nicorescu et al., 2010; Seguineau De
353 Preval, Fabrice, Gérard, & Samir, 2014a; Seguineau De Preval, Fabrice, Gilles, Gérard, & Samir,
354 2014b). This reduction is mainly due to the increased shear, elongation and inertia forces acting
355 inside the mixing-head chamber which break down larger air bubbles into smaller bubbles (Müller-
356 Fischer et al., 2007b). In addition, increasing N leads to a narrower and more uniform bubble size
357 distribution, as shown in Fig. 4.

358

359 For a given fluid and a given rotational speed, increasing the G/L ratio results in a considerable
360 reduction in bubble size (D_{32}), as shown in Fig. 4. This result is counter-intuitive since an increase in
361 G/L reduces the foam residence time (Fig. 4) in the mixing-head chamber, thus, leading to less
362 shearing of the gas-liquid dispersion. Over the range of rotor speeds studied (500 - 1750 rpm), N does
363 not affect the residence time. The residence time inside the mixing-head chamber which has a fixed
364 volume and a fixed number of rotor-stator pairs (12) can be varied only by changing the G/L ratio
365 (Eq. 13). As shown by the data in Fig. 5 and Table 3, the same value of τ corresponds to different
366 G/L ratios but the same G/L ratio may lead to different values of τ and different dispersion viscosities.
367 Hence, the effects of τ on bubble size are complicated and hard to interpret (Balerin et al., 2007; Mary
368 et al., 2013).

369

370 The reduction in bubble size caused by increasing the G/L ratio, however, can be explained by the
371 significant rise in the apparent viscosity of the dispersion inside the mixing-head chamber when the

372 G/L ratio is increased, as shown in Fig. 5. The shear rate inside the mixing-head chamber was
373 estimated using Eq. (11) and used to predict the apparent viscosity of the model fluids and gas-liquid
374 dispersion using Eq. (1). An increase in apparent viscosity enhances the shear stresses acting on the
375 bubbles leading to a reduction in bubble size (Indrawati & Narsimhan, 2008). As shown in Fig. 6,
376 foam generated from MF2 at $G/L = 1.5$ exhibits a much more uniform bubble size distribution
377 compared to foam generated at $G/L = 1.0$. Muller-Fischer et al. (2007a), using a dynamically
378 enhanced membrane foaming technique, found that an increase in air volume fraction led to a
379 reduction in bubble size which they attributed to an increase in dispersion viscosity. Similarly,
380 increasing the disperse phase volume fraction in emulsions has also been reported to lead to a
381 reduction in droplet size and polydispersity in the turbulent flow regime (Tcholakova et al., 2011;
382 Vankova et al., 2007).

383

384 *3.3.2 Effects of surfactant concentration*

385 The effects of surfactant concentration on foam bubble size are depicted in Fig. 7. Fluids MF1, MF2
386 and MF3 are identical except for their different surfactant content. For $G/L = 1.0$, a higher
387 concentration of PGE 55 from MF1 to MF2, to MF3 does not result in significant difference in mean
388 bubble size. At higher G/L values, e.g. $G/L = 1.5$, a higher surfactant concentration initially leads to a
389 much smaller bubble size (MF1 and MF2) but no further effect is observed beyond a certain
390 concentration; MF2 and MF3 have concentrations of 0.5 wt% and 1.0 wt%, respectively, but exhibit
391 the same mean bubble size at all rotational speeds. These effects are visualised in Fig. 8 showing
392 sample X-ray micro-CT images of the different foam microstructures. This bubble size behaviour has
393 previously been reported for Newtonian fluids (Seguineau De Preval et al., 2014a; Seguineau De
394 Preval et al., 2014b). The same trend was followed by the volume gas fraction, as discussed above.

395

396 As shown in Fig. 9, changing the surfactant concentration alters the surface tension kinetics especially
397 at short time scales similar to the processing times (<100 s). At higher PGE 55 concentrations up to ~
398 0.5 wt%, the higher availability of surfactant molecules and their ability to diffuse faster to the air-
399 water interfaces leads to the formation of smaller bubbles. Thereafter, the solution is saturated with
400 surfactant and more PGE 55 produces no effect on surface tension kinetics and, hence, bubble size.

401

402 *3.3.3 Effects of Xanthan gum concentration*

403 A higher XG concentration leads to a reduction in foam bubble size at all rotor speeds, but beyond a
404 certain value the effect becomes negligible, as visualised in the images of Fig. 10 and represented in
405 the mean bubble size plots in Fig. 11a. This has also been previously observed for foams generated
406 from Newtonian fluids (Mary et al., 2013; Seguineau De Preval et al., 2014a; Seguineau De Preval et
407 al., 2014b) and non-Newtonian shear-thinning fluids (Balerin et al., 2007; Hanselmann & Windhab,
408 1998; Indrawati & Narsimhan, 2008).

409

410 There are two competing factors which are affected by changing the XG concentration, namely the
411 apparent viscosity and the surface tension kinetics, as shown in Figs. 11b and 11c, respectively. As
412 discussed above, a higher dispersion viscosity arising from a higher XG content can, up to a point,
413 lead to a finer foam texture in the mixing-head chamber due to higher shear stresses which produce
414 smaller bubbles and slower drainage which prevents bubble coalescence (Indrawati & Narsimhan,
415 2008). At the same time, the slower surface tension kinetics arising from a higher XG content, up to a
416 point, lead to the formation of larger bubbles since the surfactant diffuses more slowly to air-water
417 interfaces. The results obtained here indicate that the viscosity effects are predominant.

418

419 **3.4 Theoretical analysis**

420 *3.4.1 Data reduction for interpretation of bubble size*

421 The above results can be generalised by interpreting the data in terms of the Weber number, a ratio of
422 shear forces to capillary pressure acting on the bubble. Typical apparent viscosity curves of the model
423 fluids used and the foams produced are represented in Fig. 12. As pointed out above, the Cross model
424 (Eq. 1) used to represent the apparent viscosity curves of the foam can be reduced in the central shear-
425 thinning region ($\eta_{\infty} \ll \eta < \eta_0$) which covers the entire experimental conditions of this study to the
426 much simpler two-parameter power law model:

427

$$428 \quad \eta = k\dot{\gamma}^{n-1} \quad (14)$$

429

430 where k is the consistency index, n is the flow behaviour index. This facilitates the definition of a
431 modified critical Weber number, thus:

432

$$433 \quad We = \frac{k(ND)^n}{\sigma_e s^{n-1}} \quad (15)$$

434

435 where σ_e is the equilibrium surface tension value reached after at least one hour (Fig. 9).

436

437 Different authors have adopted different definitions of We for foam taking into consideration the
438 geometrical dimensions of the foam generating device, the hydrodynamics and liquid composition. A
439 constant value of 0.24–0.60 is commonly reported for the critical Weber number at which bubbles
440 rupture (Balerin et al., 2007; Kroezen et al., 1988; Thakur, Vial, & Djelveh, 2005). Thakur et al.
441 (2003), however, using time and shear rate dependent non-Newtonian liquids in a mechanical agitator
442 device, found that We increased as a function of rotor speed. Similarly, using a continuous rotor-
443 stator device and Newtonian media, Balerin et al. (2007) reported the same result; the increase in this
444 case was attributed to a rise in local heat dissipation at higher rotor speeds.

445

446 The variations of foam mean bubble size are plotted in Fig. 13 as a function of We for the various
447 experimental conditions investigated including all G/L ratios. The data follow the same general trend
448 showing D_{32} decreasing with We (Fig. 13a). The best line fitted through the data shows, however, a
449 significant amount of scatter ($\pm 20\%$). When the data are plotted for $G/L \geq 1.5$ only, in Fig. 13b, the
450 data collapse on a single line with much little scatter ($\pm 10\%$). This can be explained by the fact that
451 data for $G/L = 1.0$ correspond to an inertial turbulent flow regime where the eddy scale is smaller than
452 the bubble size and, hence, do not fit in with data for $G/L > 1.5$ which correspond to a viscous turbulent
453 flow regime where the eddies are larger than the bubble size. It is interesting to note that if the results
454 for MF2, M4 and MF5 at $G/L = 1.5$, with the same surfactant concentration but a lower XG
455 concentration, are plotted separately (Fig. 13c), the data collapse on a single line with little scatter (\pm
456 5%). Indrawati and Narsimhan (2008) reported similar observations using a mechanically agitated
457 vessel to generate their foam, but this result is hard to explain.

458

459 Overall, these findings show that a general (approximately) unified curve can be obtained with such
460 complex systems which, when produced for one fluid formulation, could be used to interpret data of
461 foams in different non-Newtonian media. This result should simplify the prediction of foam texture.

462

463 3.4.2 *Effects of energy input on foam microstructure*

464 The energy input during the production of foam using a continuous rotor-stator is an important
465 parameter for process design and optimisation. For a given fluid formulation and a fixed rotor-stator
466 geometry, energy dissipation inside the mixing-head chamber can be controlled by either changing the
467 rotational speed or the G/L ratio. The rotor speed affects the shear stresses acting within the mixing-
468 head chamber, whereas G/L ratio controls the residence time (τ), and both parameters impact the
469 bubble size distribution and, hence, the microstructure of the foam. Thus, the effects of N and G/L on
470 gas volume fraction and bubble size distribution were investigated.

471

472 Typical variations of the net volumetric energy input (E_v) with N and G/L ratio are depicted in Fig. 14
473 for foams produced from fluid MF2. As expected, for a given G/L ratio, E_v increases exponentially
474 as a function of N . As G/L increases (and hence τ reduces), E_v diminishes considerably. Hence,
475 generating foams with a higher gas fraction requires less energy input. Bubble size, on the other
476 hand, follows an exponential decay as more energy is dissipated inside the mixing-head chamber (Fig.
477 15). As previously pointed out, increasing the G/L ratio increases the apparent viscosity of the
478 dispersion which enhances the shear forces inside the mixing-head chamber to break down larger air
479 bubbles into smaller bubbles. Thus, for a given amount of energy dissipation, a higher G/L ratio leads
480 to a smaller bubble size. Hence, for a given E_v , a higher G/L ratio results in a higher gas fraction and
481 a smaller bubble size, i.e. a richer foam with a finer texture.

482

483 **3.5 Foam stability**

484 Static foam stability is governed by the combined effects of foam drainage, collapse and coarsening.
485 Foam drainage and collapse were measured over a long period of time (~ 1300 hr) by monitoring
486 foam samples collected at the outlet of the rotor-stator device and stored in a controlled environment.
487 Foam drainage and collapse profiles are shown in Fig. 16 for MF2 at $G/L = 1.0$. In general, both
488 drainage and collapse are very slow indicating that the foams are very stable. Foams produced at
489 higher rotor speeds exhibit slower drainage. As discussed above, increasing N leads to a significant
490 reduction in bubble size and a narrower bubble size distribution. This results in an increase in foam
491 stability due to the higher liquid flow resistance through the thinner lamellae and Plateau borders
492 network (Nicorescu et al., 2010). The use of XG imparts non-Newtonian characteristics to the
493 continuous phase including a high zero-shear Newtonian viscosity (Fig. 12; sometimes confused in
494 the literature with the existence of a yield stress) which counters gravitational drainage and gives high
495 stability to the foam. In addition, PGE 55 can form multilamellar vesicles in the liquid which can
496 significantly hinder liquid drainage by obstructing the Plateau borders (Curschellas et al., 2012a; C.
497 Curschellas et al., 2012b; Curschellas et al., 2013). Therefore, higher XG or PGE 55 concentrations
498 improve foam stability. Furthermore, increasing the G/L ratio, as discussed above, increases the air
499 volume fraction which reduces the liquid contained within the foam (Plateau borders and lamellae)
500 and the foam stability is enhanced (data not shown). For example, at $G/L = 1.5$, the rate of drainage is
501 slowed down by an order of magnitude and no foam collapse is observed within 1300 hr.

502

503 Foam coarsening was assessed over several weeks via X-ray micro-CT using similar foam samples, as
504 shown in Fig. 17. The use of the non-ionic surfactant PGE 55 provided excellent resistance to bubble
505 coalescence as its molecules/vesicles irreversibly adsorb at gas-liquid interfaces (Curschellas et al.,
506 2013). Foam coarsening was found to be generally slow. Foams generated at higher rotor speeds had
507 finer bubbles (i.e. faster air diffusion and disproportionation) and thinner foam lamellae (i.e. more
508 coalescence) which led to faster foam coarsening. Whilst high G/L ratios lead to slower drainage and
509 collapse, they undergo faster coarsening (data not shown) due to their thinner lamellae separating the
510 neighbouring bubbles. It is also known that PGE 55 can irreversibly adsorb to an air-water interface
511 and hence provide steric stabilisation against bubble coalescence (Duerr-Auster, Gunde, Mäder, &
512 Windhab, 2009).

513

514 **4. Conclusions**

515 This study focused on the production of foams from viscous shear-thinning liquids using a pilot-scale
516 continuous multi rotor-stator device operating at atmospheric pressure. The effects of process
517 parameters (rotor speed, G/L ratio) and liquid formulation (surfactant concentration, Xanthan gum
518 concentration) on foam gas volume fraction and bubble size distribution were studied. Rotor speed
519 and G/L ratio were the dominant factors in determining the gas volume fraction and bubble size

520 distribution. Higher rotor speed which implies higher energy input, led to finer texture foams.
 521 Increasing the G/L ratio led to a reduction in average residence time but, counter-intuitively, reduced
 522 foam bubble size and polydispersity. This was attributed to an increase in the apparent viscosity of
 523 the dispersion which in turn enhances the shear forces inside the mixing-head chamber to break down
 524 larger air bubbles into smaller bubbles. Hence, for a given energy input, a higher G/L ratio results in
 525 a higher gas fraction and a smaller bubble size, i.e. a richer foam with a finer texture. The foams
 526 produced exhibited a high static stability over long periods of time. Higher rotor speeds and G/L
 527 ratios resulted in slower drainage and collapse, but foam coarsening was faster.

528

529 **Acknowledgements**

530 Saifullah Jabarkhyl's PhD research was funded by EPSRC and Unilever Colworth (UK).

531

532 **Notation**

533	D	rotor diameter (m)
534	d	bubble diameter (m)
535	D_{32}	sauter mean diameter (m)
536	E_V	specific energy per m^3 of foam processed ($J m^{-3}$)
537	f	correlation factor (-)
538	F	frequency (%)
539	h	number of rotor-stator pairs (-)
540	h_f	foam collapse (m)
541	I	number of pins on rotor (-)
542	k	consistency index ($Pa s^n$)
543	L	diameter of annulus mixing space (m)
544	MF1	model fluid 1 (-)
545	MF2	model fluid 2 (-)
546	MF3	model fluid 3 (-)
547	MF4	model fluid 4 (-)
548	MF5	model fluid 5 (-)
549	N	rotational speed (s^{-1})
550	n	flow behaviour index (-)
551	n_i	number of bubble with diameter i (-)
552	o	width of rotor pin (m)
553	$P_{v,diss}$	net volumetric power input ($J s^{-1} m^{-3}$)
554	P_0	Power number (-)
555	P_0^*	generalised Power number (-)
556	PGE 55	polyglycerol ester of fatty acid (-)

557	q	height of rotor/stator pin (m)
558	Q_L	liquid volumetric flowrate (m ³ s ⁻¹)
559	Q_G	gas volumetric flowrate (m ³ s ⁻¹)
560	Re	Reynolds number (-)
561	Re^*	generalised Reynolds number (-)
562	s	distance between rotor-stator (m)
563	V	volume of mixing-head chamber (m ³)
564	v_L	liquid drained (m ³)
565	We	Weber number (-)
566	XG	Xanthan gum (-)
567	X-ray micro-CT	X-ray micro-Computed Tomography (-)
568	$z = \frac{\pi D}{I}$	distance between rotor pins (m)
569		
570	<i>Greek symbols</i>	
571	τ	average residence time (s)
572	η	apparent viscosity (Pa.s)
573	ρ	density (kg m ⁻³)
574	σ	surface tension (N m ⁻¹)
575	\emptyset	air volume fraction (-)
576	$\dot{\gamma}$	shear rate (s ⁻¹)

577

578

579 **References**

- 580 Balerin, C., Aymard, P., Ducept, F., Vaslin, S., & Cuvelier, G. (2007). Effect of
581 formulation and processing factors on the properties of liquid food
582 foams. *Journal of Food Engineering*, 78(3), 802-809.
583 doi:<http://doi.org/10.1016/j.jfoodeng.2005.11.021>
- 584 Barigou, M., & Douaire, M. (2013). 9 - X-ray micro-computed tomography for
585 resolving food microstructures. In V. J. Morris & K. Groves (Eds.), *Food*
586 *Microstructures* (pp. 246-272): Woodhead Publishing.
- 587 Bikerman, J. J. (1973). *Foams*. New York: Springer-Verlag.
- 588 Campbell, G. M., & Mougeot, E. (1999). Creation and characterisation of
589 aerated food products. *Trends in Food Science & Technology*, 10(9), 283-
590 296. doi:[http://doi.org/10.1016/S0924-2244\(00\)00008-X](http://doi.org/10.1016/S0924-2244(00)00008-X)
- 591 Cox, A. R., Aldred, D. L., & Russell, A. B. (2009). Exceptional stability of food
592 foams using class II hydrophobin HFBII. *Food Hydrocolloids*, 23(2), 366-
593 376. doi:<https://doi.org/10.1016/j.foodhyd.2008.03.001>

594 Curschellas, C., Gunes, D. Z., Deyber, H., Watzke, B., Windhab, E., & Limbach, H.
595 J. (2012a). Interfacial aspects of the stability of polyglycerol ester covered
596 bubbles against coalescence. *Soft Matter*, 8(46), 11620-11631.
597 doi:10.1039/C2SM26446C

598 Curschellas, C., Keller, R., Berger, R., Rietzler, U., Fell, D., Butt, H.-J., & Limbach,
599 H. J. (2012b). Scanning force microscopy as a tool to investigate the
600 properties of polyglycerol ester foams. *Journal of Colloid and Interface*
601 *Science*, 374(1), 164-175. doi:<https://doi.org/10.1016/j.jcis.2012.01.031>

602 Curschellas, C., Kohlbrecher, J., Geue, T., Fischer, P., Schmitt, B., Rouvet, M., . . .
603 Limbach, H. J. (2013). Foams Stabilized by Multilamellar Polyglycerol Ester
604 Self-Assemblies. *Langmuir*, 29(1), 38-49. doi:10.1021/la3029116

605 Duerr-Auster, N., Eisele, T., Wepf, R., Gunde, R., & Windhab, E. J. (2008).
606 Influence of pH on colloidal properties and surface activity of polyglycerol
607 fatty acid ester vesicles. *Journal of Colloid and Interface Science*, 327(2),
608 446-450. doi:<http://doi.org/10.1016/j.jcis.2008.08.047>

609 Duerr-Auster, N., Gunde, R., Mäder, R., & Windhab, E. J. (2009). Binary
610 coalescence of gas bubbles in the presence of a non-ionic surfactant.
611 *Journal of Colloid and Interface Science*, 333(2), 579-584.
612 doi:<http://doi.org/10.1016/j.jcis.2009.01.016>

613 Germain, J. C., & Aguilera, J. M. (2014). Multi-scale properties of protein-
614 stabilized foams. *Food Structure*, 1(1), 55-70.
615 doi:<https://doi.org/10.1016/j.foostr.2014.01.001>

616 Guo, E., Zeng, G., Kazantsev, D., Rockett, P., Bent, J., Kirkland, M., . . . Lee, P. D.
617 (2017). Synchrotron X-ray tomographic quantification of microstructural
618 evolution in ice cream – a multi-phase soft solid. *RSC Advances*, 7(25),
619 15561-15573. doi:10.1039/C7RA00642J

620 Hanselmann, W., & Windhab, E. (1998). Flow characteristics and modelling of
621 foam generation in a continuous rotor/stator mixer. *Journal of Food*
622 *Engineering*, 38(4), 393-405. doi:[http://dx.doi.org/10.1016/S0260-](http://dx.doi.org/10.1016/S0260-8774(98)00129-0)
623 [8774\(98\)00129-0](http://dx.doi.org/10.1016/S0260-8774(98)00129-0)

624 Indrawati, L., & Narsimhan, G. (2008). Characterization of protein stabilized
625 foam formed in a continuous shear mixing apparatus. *Journal of Food*
626 *Engineering*, 88(4), 456-465.
627 doi:<http://doi.org/10.1016/j.jfoodeng.2008.03.003>

628 Jang, W., Nikolov, A., Wasan, D. T., Chen, K., & Campbell, B. (2005). Prediction of
629 the Bubble Size Distribution during Aeration of Food Products. *Industrial*
630 *& Engineering Chemistry Research*, 44(5), 1296-1308.
631 doi:10.1021/ie049740x

632 Kroezen, A. B. J., Groot Wassink, J., & Bertlein, E. (1988). Foam generation in a
633 rotor—stator mixer: schaumzeugung in einem rotor—stator mischer.

634 *Chemical Engineering and Processing: Process Intensification*, 24(3), 145-
635 156. doi:[https://doi.org/10.1016/0255-2701\(88\)80018-7](https://doi.org/10.1016/0255-2701(88)80018-7)

636 Kroezen, A. B. J., & Wassink, J. G. (1987). Bubble size distribution and energy
637 dissipation in foam mixers. *Journal of the Society of Dyers and Colourists*,
638 103(11), 386-394. doi:10.1111/j.1478-4408.1987.tb01090.x

639 Kulmyrzaev, A., Cancelliere, C., & McClements, D. J. (2000). Characterization of
640 aerated foods using ultrasonic reflectance spectroscopy. *Journal of Food*
641 *Engineering*, 46(4), 235-241. doi:[http://doi.org/10.1016/S0260-](http://doi.org/10.1016/S0260-8774(00)00070-4)
642 [8774\(00\)00070-4](http://doi.org/10.1016/S0260-8774(00)00070-4)

643 Lim, K. S., & Barigou, M. (2004). X-ray micro-computed tomography of cellular
644 food products. *Food Research International*, 37(10), 1001-1012.
645 doi:<https://doi.org/10.1016/j.foodres.2004.06.010>

646 Mary, G., Mezdour, S., Delaplace, G., Lauhon, R., Cuvelier, G., & Ducept, F.
647 (2013). Modelling of the continuous foaming operation by dimensional
648 analysis. *Chemical Engineering Research and Design*, 91(12), 2579-2586.
649 doi:<http://doi.org/10.1016/j.cherd.2013.05.020>

650 Mezdour, S., Séguineau de Préval, E., Granda, P., Cuvelier, G., & Ducept, F.
651 (2017). *Impact of Interfacial Characteristics on Foam Structure: Study on*
652 *Model Fluids and at Pilot Scale* (Vol. 72).

653 Müller-Fischer, N., Bleuler, H., & Windhab, E. J. (2007a). Dynamically enhanced
654 membrane foaming. *Chemical Engineering Science*, 62(16), 4409-4419.
655 doi:<https://doi.org/10.1016/j.ces.2007.05.026>

656 Müller-Fischer, N., Suppiger, D., & Windhab, E. J. (2007b). Impact of static
657 pressure and volumetric energy input on the microstructure of food foam
658 whipped in a rotor–stator device. *Journal of Food Engineering*, 80(1), 306-
659 316. doi:<http://doi.org/10.1016/j.jfoodeng.2006.05.026>

660 Müller-Fischer, N., & Windhab, E. J. (2005). Influence of process parameters on
661 microstructure of food foam whipped in a rotor–stator device within a
662 wide static pressure range. *Colloids and Surfaces A: Physicochemical and*
663 *Engineering Aspects*, 263(1–3), 353-362.
664 doi:<http://doi.org/10.1016/j.colsurfa.2004.12.057>

665 Narchi, I., Vial, C., Labbafi, M., & Djelveh, G. (2011). Comparative study of the
666 design of continuous aeration equipment for the production of food
667 foams. *Journal of Food Engineering*, 102(2), 105-114.
668 doi:<http://doi.org/10.1016/j.jfoodeng.2010.07.030>

669 Nicorescu, I., Vial, C., Loisel, C., Riaublanc, A., Djelveh, G., Cuvelier, G., &
670 Legrand, J. (2010). *Influence of protein heat treatment on the continuous*
671 *production of food foams* (Vol. 43).

672 Pugh, R. J. (2016). Generation of bubbles and foams. In R. J. Pugh (Ed.), *Bubble*
673 *and Foam Chemistry* (pp. 155-193). Cambridge: Cambridge University
674 Press.

- 675 Seguineau De Preval, E., Fabrice, D., Gérard, C., & Samir, M. (2014a). Effect of
676 bulk viscosity and surface tension kinetics on structure of foam generated
677 at the pilot scale. *Food Hydrocolloids*, 34, 104-111.
678 doi:<http://doi.org/10.1016/j.foodhyd.2012.12.001>
- 679 Seguineau De Preval, E., Fabrice, D., Gilles, M., Gérard, C., & Samir, M. (2014b).
680 Influence of surface properties and bulk viscosity on bubble size
681 prediction during foaming operation. *Colloids and Surfaces A:
682 Physicochemical and Engineering Aspects*, 442, 88-97.
683 doi:<http://doi.org/10.1016/j.colsurfa.2013.05.025>
- 684 Tcholakova, S., Lesov, I., Golemanov, K., Denkov, N. D., Judat, S., Engel, R., &
685 Danner, T. (2011). Efficient Emulsification of Viscous Oils at High Drop
686 Volume Fraction. *Langmuir*, 27(24), 14783-14796.
687 doi:10.1021/la203474b
- 688 Thakur, R. K., Vial, C., & Djelveh, G. (2005). Combined effects of process
689 parameters and composition on foaming of dairy emulsions at low
690 temperature in an agitated column. *Journal of Food Engineering*, 68(3),
691 335-347. doi:<https://doi.org/10.1016/j.jfoodeng.2004.06.008>
- 692 Vankova, N., Tcholakova, S., Denkov, N. D., Ivanov, I. B., Vulchev, V. D., &
693 Danner, T. (2007). Emulsification in turbulent flow 1. Mean and maximum
694 drop diameters in inertial and viscous regimes. *J Colloid Interface Sci*,
695 312(2), 363-380. doi:10.1016/j.jcis.2007.03.059
- 696 Walstra, P. (1989). *Principles of Foam Formation and Stability*, London.
- 697

Table 1. Model fluids composition and properties.

Model fluid	PGE 55 (wt%)	XG (wt%)	Sugar (wt%)	σ_e (mN m ⁻¹)	η_o (Pa s)	η_∞ (Pa s)	c (-)	m (-)	R^2 (-)
MF1	0.2	0.50	25	39	85	0.009	30.00	0.82	0.993
MF2	0.5	0.50	25	38	116	0.010	33.72	0.83	0.993
MF3	1.0	0.50	25	38	135	0.009	30.00	0.83	0.996
MF4	0.5	0.25	25	38	10	0.010	20.00	0.70	0.992
MF5	0.5	0.35	25	38	35	0.010	28.00	0.75	0.998

Table 2. Geometrical dimensions of continuous rotor-stator device.

Parameter	Symbol (unit)	Value
Diameter of annulus mixing space	L (mm)	5.00
Number of pins on rotor	I (-)	13.00
Number of rotor-stator pairs	h (-)	12.00
Distance between rotor-stator	s (mm)	1.00
Height of rotor/stator pin	q (mm)	2.50
Width of rotor pin	o (mm)	4.70
Rotor diameter	D (mm)	50.00
Distance between rotor pins	z (mm)	12.08

Table 3. Effects of experimental conditions on experimental gas volume fraction (Sample ϕ_e data shown here for cases where $Q_L = 5 \text{ L hr}^{-1}$ and $Q_G = 5, 7.5$ and 10.0 L hr^{-1}).

N (rpm)	MF1		MF2			MF3		MF4		MF5	
	G/L = 1.0 ($\tau = 31 \text{ s}$)	G/L = 1.5 ($\tau = 25 \text{ s}$)	G/L = 1.0 ($\tau = 31 \text{ s}$)	G/L = 1.5 ($\tau = 25 \text{ s}$)	G/L = 2.0 ($\tau = 20 \text{ s}$)	G/L = 1.0 ($\tau = 31 \text{ s}$)	G/L = 1.5 ($\tau = 25 \text{ s}$)	G/L = 1.0 ($\tau = 31 \text{ s}$)	G/L = 1.5 ($\tau = 25 \text{ s}$)	G/L = 1.0 ($\tau = 31 \text{ s}$)	G/L = 1.5 ($\tau = 25 \text{ s}$)
500	0.52	blow-by	0.52	0.62	blow-by	0.51	0.61	0.51	0.61	0.52	0.62
750	0.53	blow-by	0.52	0.63	blow-by	0.51	0.61	0.52	0.61	0.52	0.62
1000	0.53	0.63	0.52	0.63	0.69	0.51	0.61	0.51	0.61	0.52	0.62
1250	0.53	0.63	0.52	0.63	0.69	0.52	0.61	0.52	0.61	0.52	0.62
1500	0.54	0.63	0.52	0.63	0.69	0.53	0.61	0.52	0.62	0.53	0.63
1750	0.54	0.63	0.52	0.63	0.69	0.53	0.61	0.53	0.62	0.52	0.63

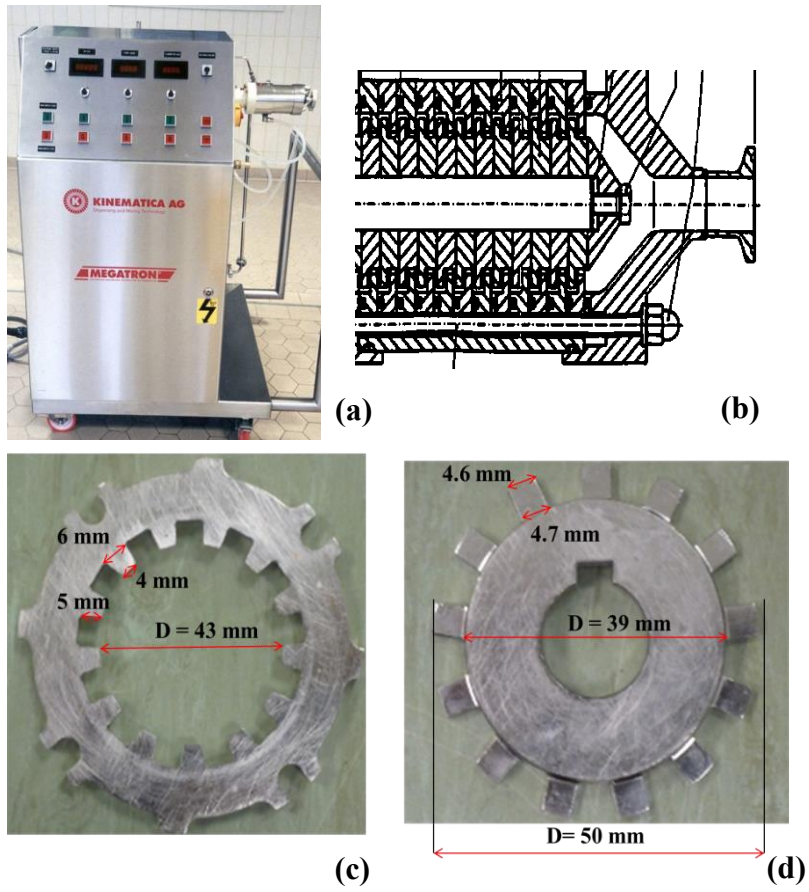


Fig. 1. Foam generator: (a) pilot-scale continuous rotor-stator unit; (b) schematic of mixing-head chamber; (c) stator; (d) rotor.

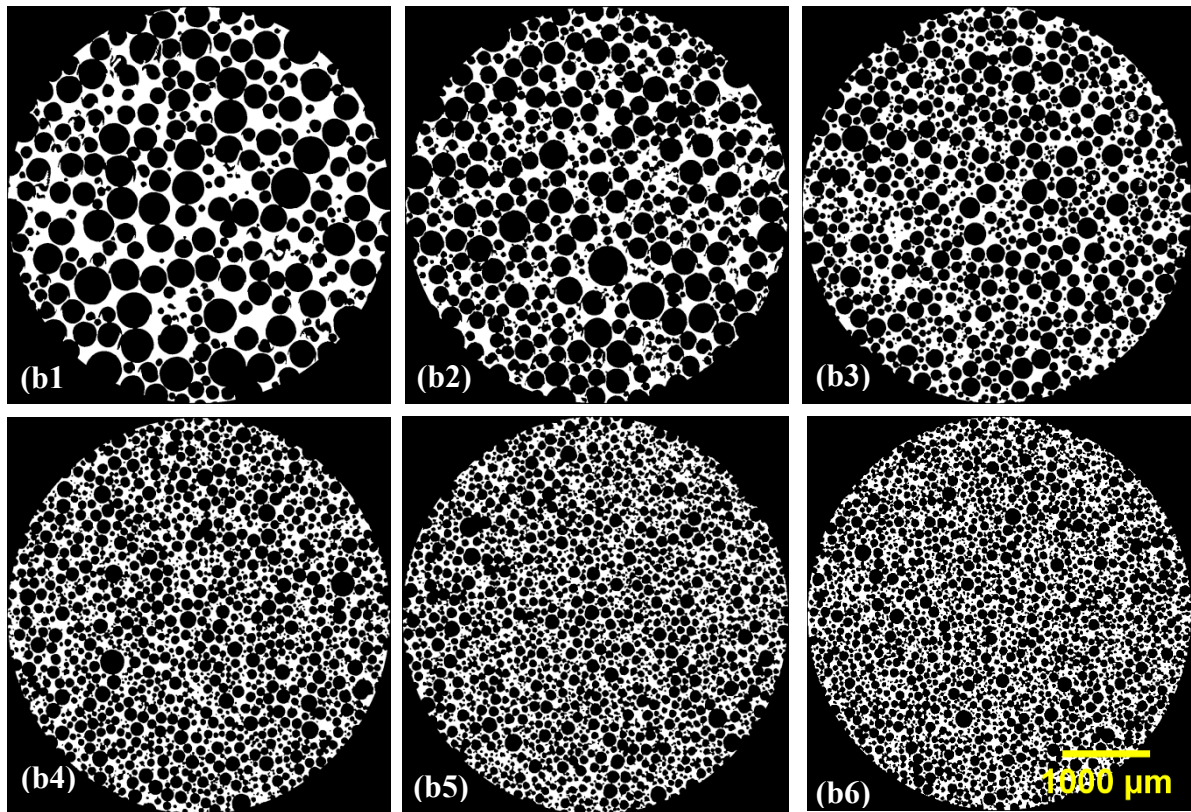
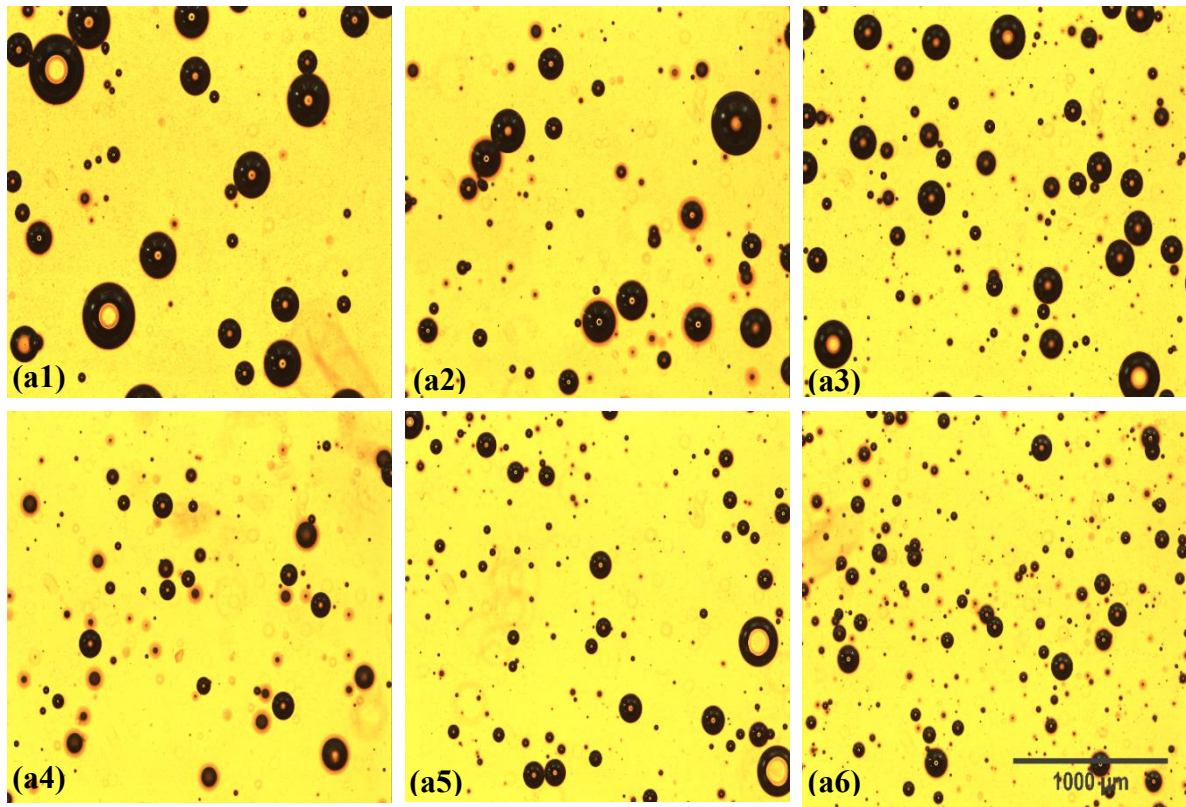


Fig. 2. Foam images obtained using: a digital microscope (a1-a6); and X-ray micro-CT technique (2D slices) (b1-b6). Fluid MF2; $G/L = 1.5$; $N = 500, 750, 1000, 1250, 1500, 1750$ rpm, respectively.

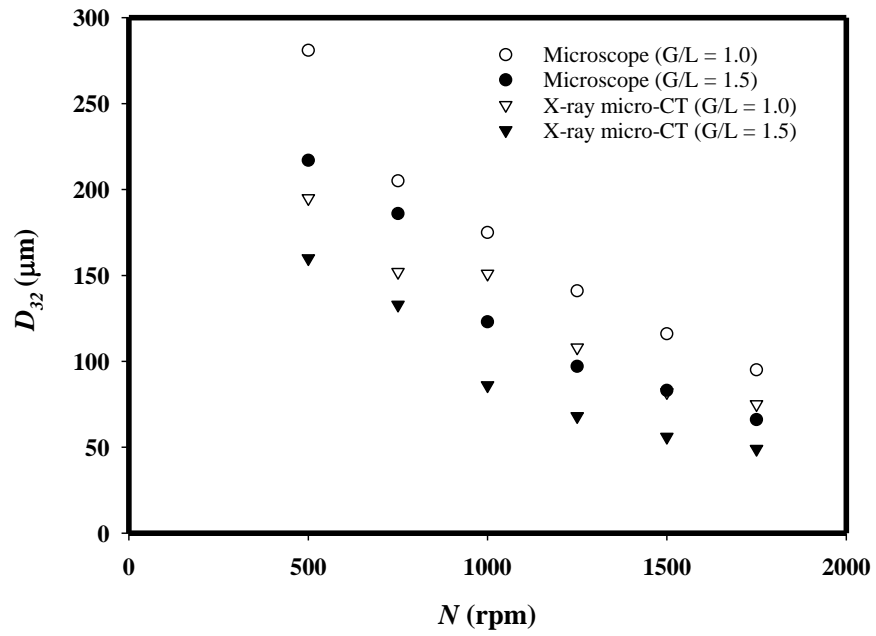


Fig. 3. Comparison of D_{32} obtained from light microscopy and X-ray micro-CT techniques for MF2.

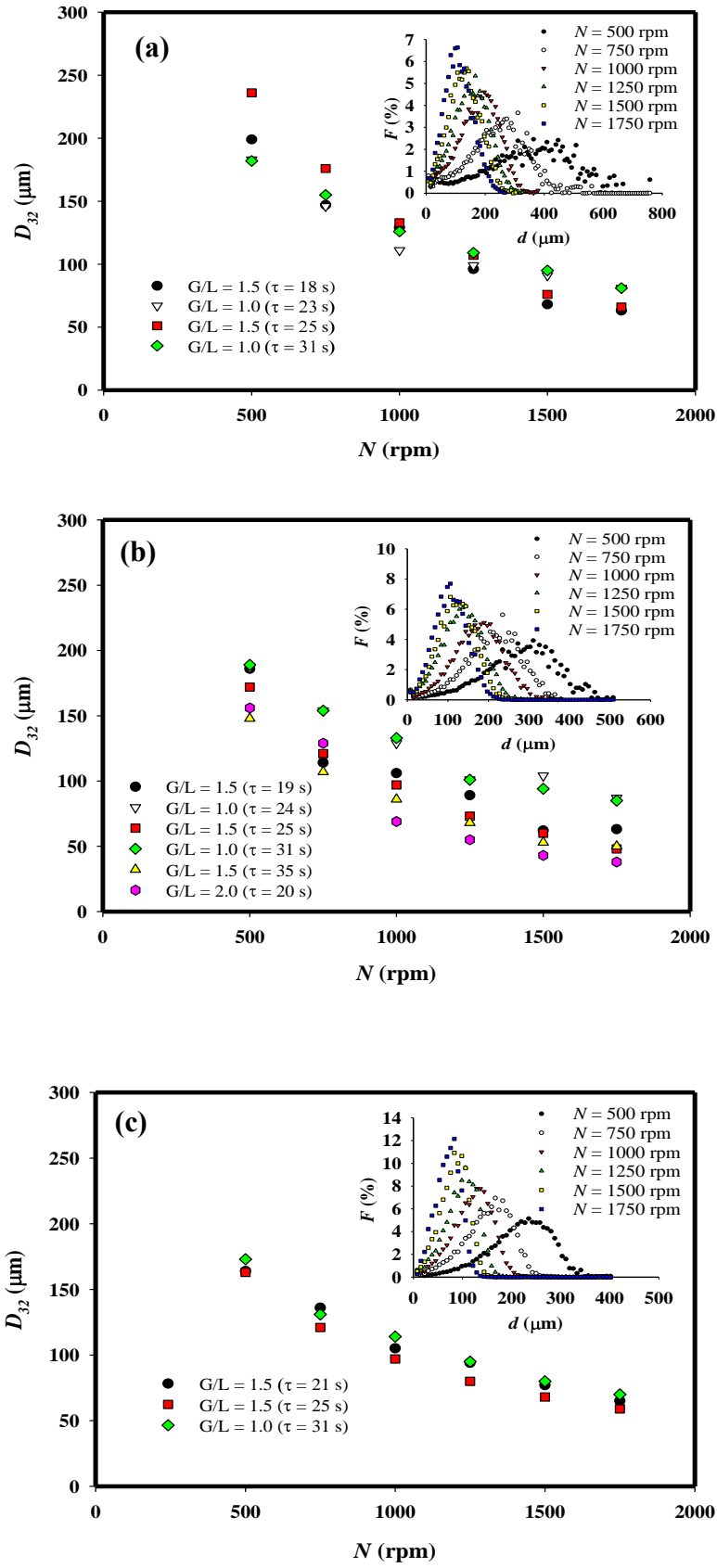


Fig. 4. Effects of rotational speed and G/L ratio on D_{32} : (a) MF1; (b) MF2; and (c) MF3.

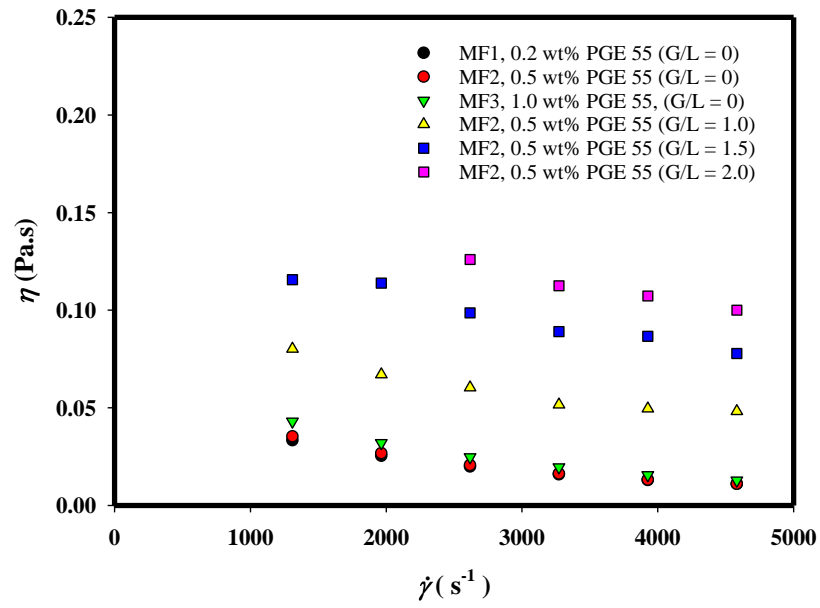


Fig. 5. Variation of apparent viscosity (Eq. 1) of gas-liquid dispersion inside mixing-head chamber and of model fluids under the same process conditions of shear (Eq. 11).

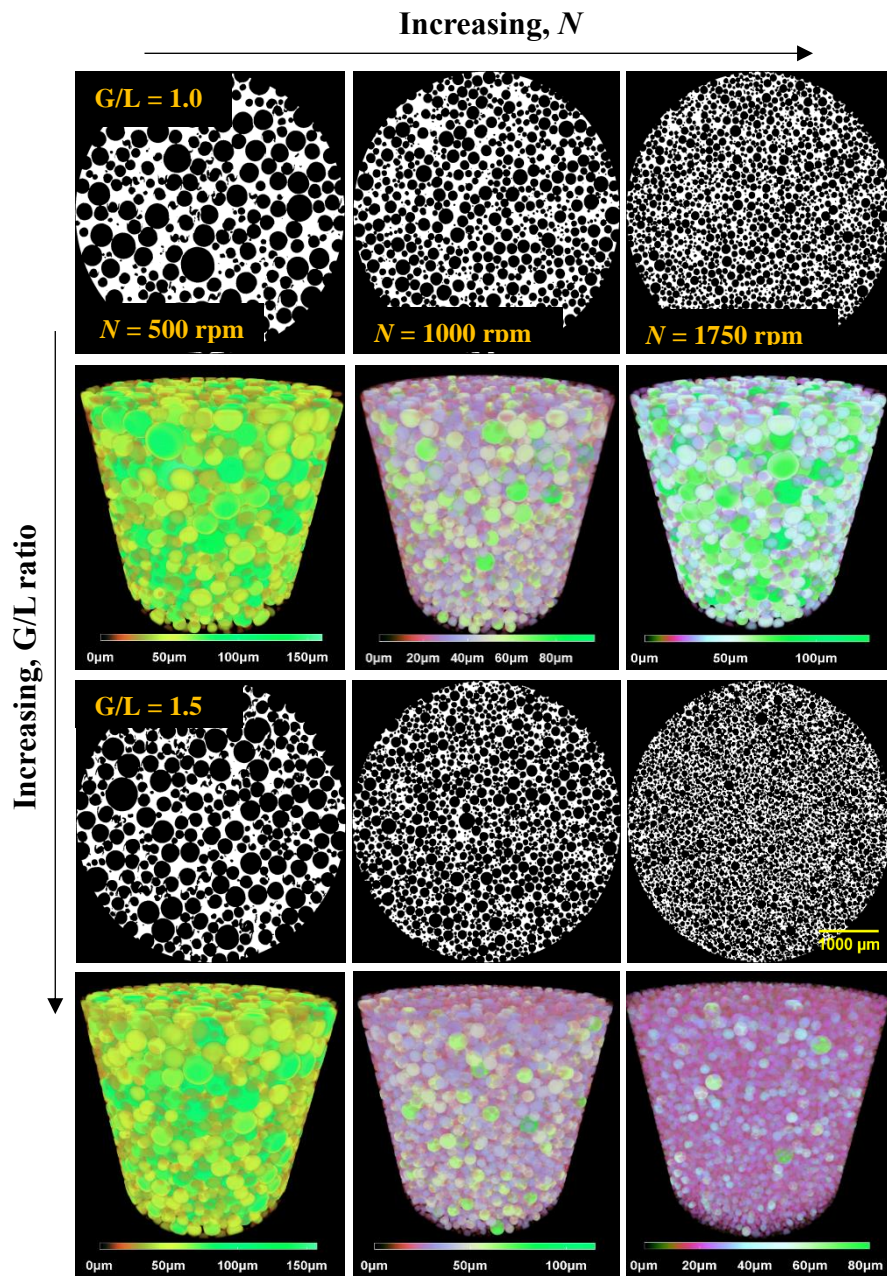


Fig. 6. Rendered 3D X-ray micro-CT model of foam generated from MF2 numerically cut to reveal its inner structure.

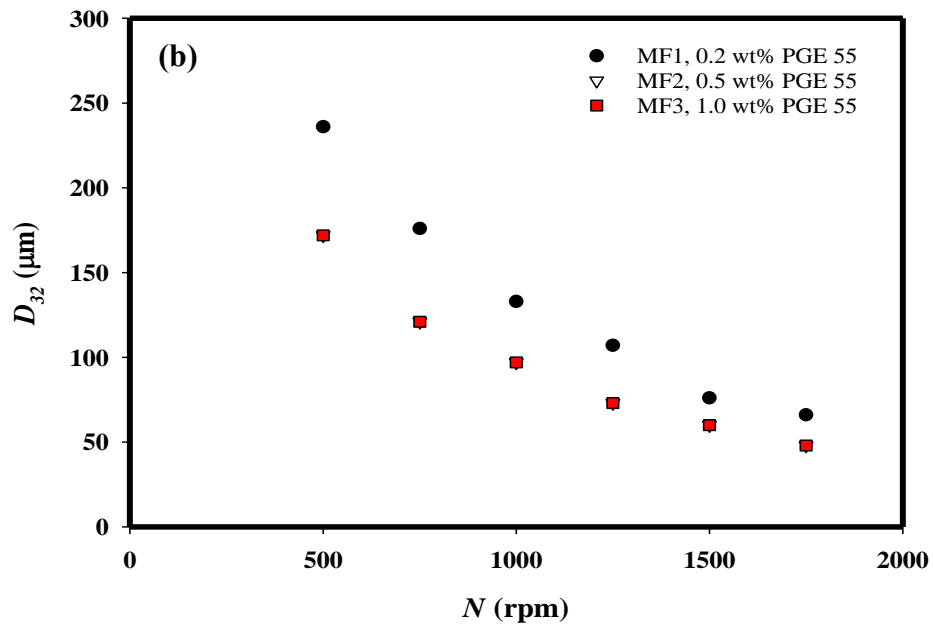
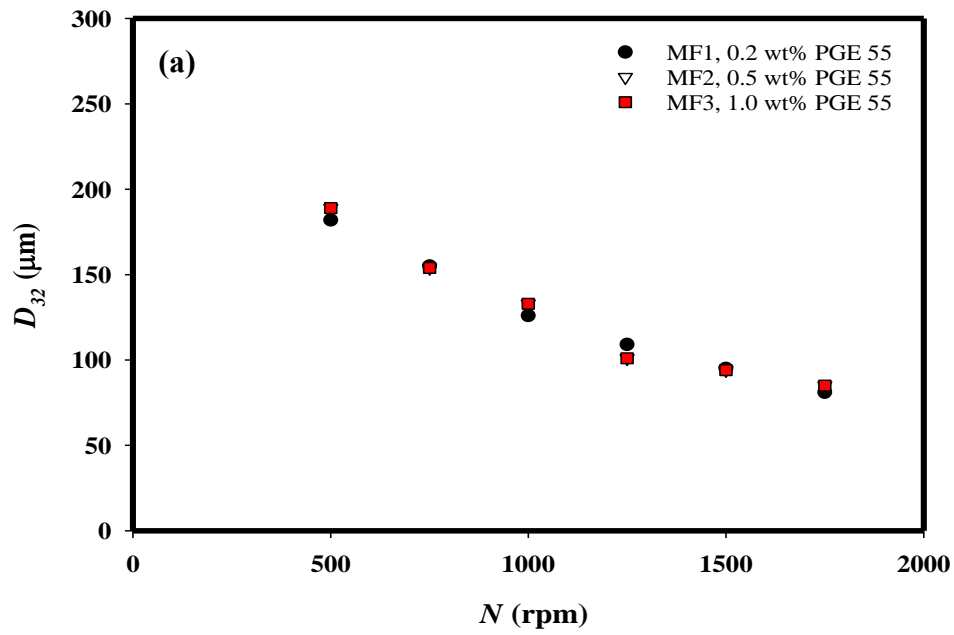


Fig. 7. Effects of surfactant concentration on D_{32} : (a) $G/L = 1.0$; (b) $G/L = 1.5$.

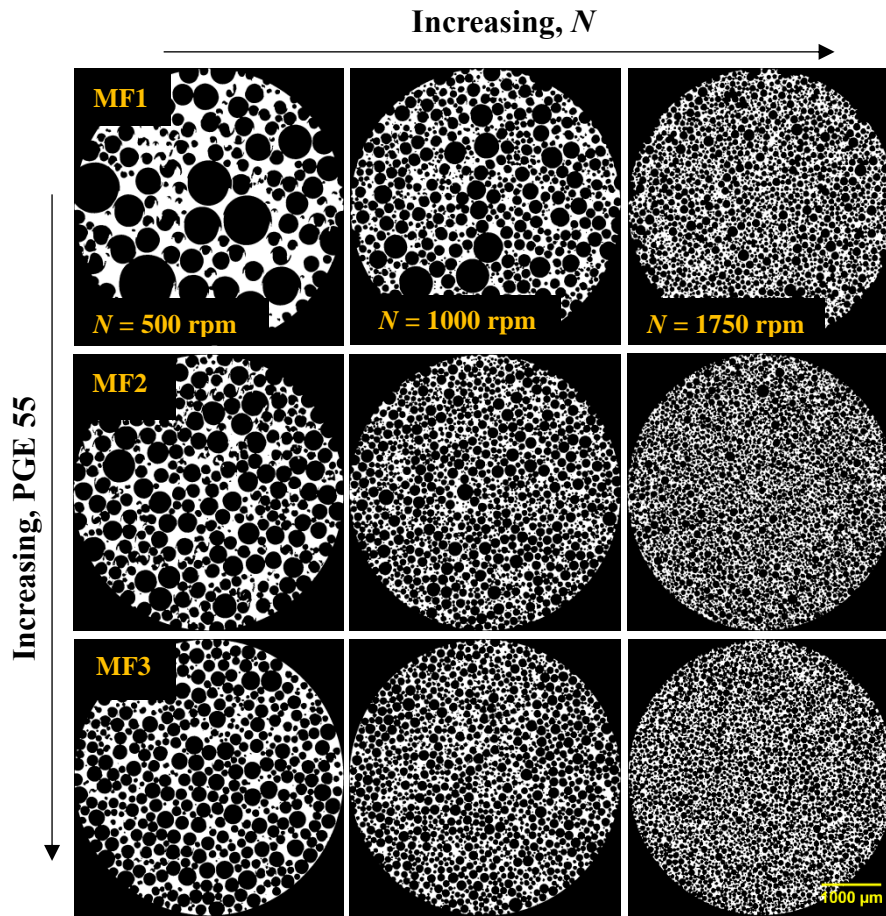


Fig. 8. X-ray micro-CT images of foam samples generated from MF1, MF2 and MF3 at $G/L = 1.5$.

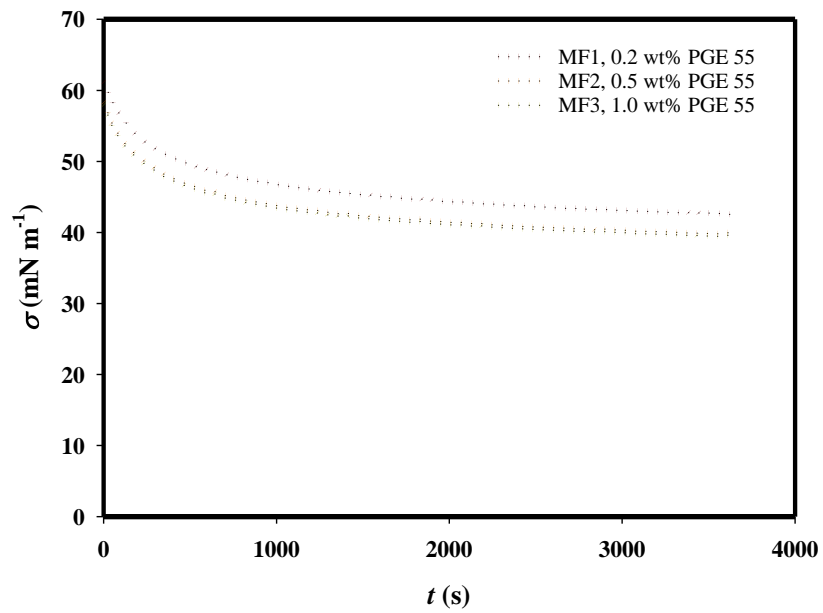


Fig. 9. Dynamics surface tension isotherm of model fluids.

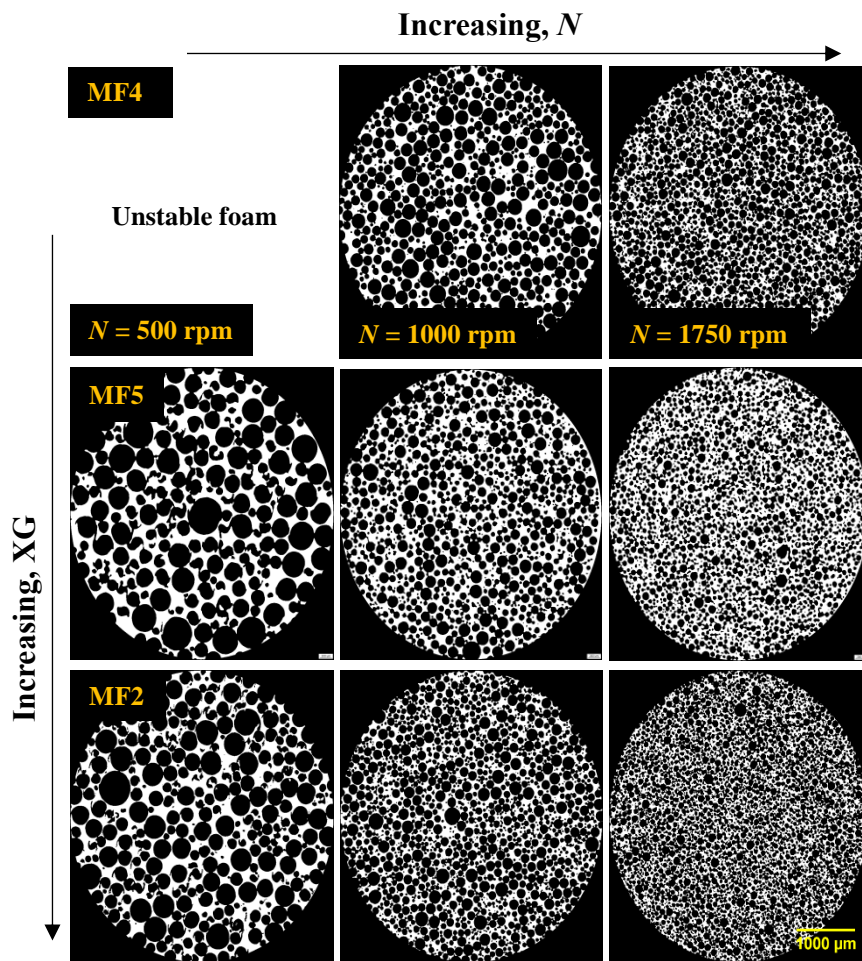


Fig. 10. X-ray micro-CT images of foam samples generated from MF2, MF4 and MF5 at $G/L = 1.5$.

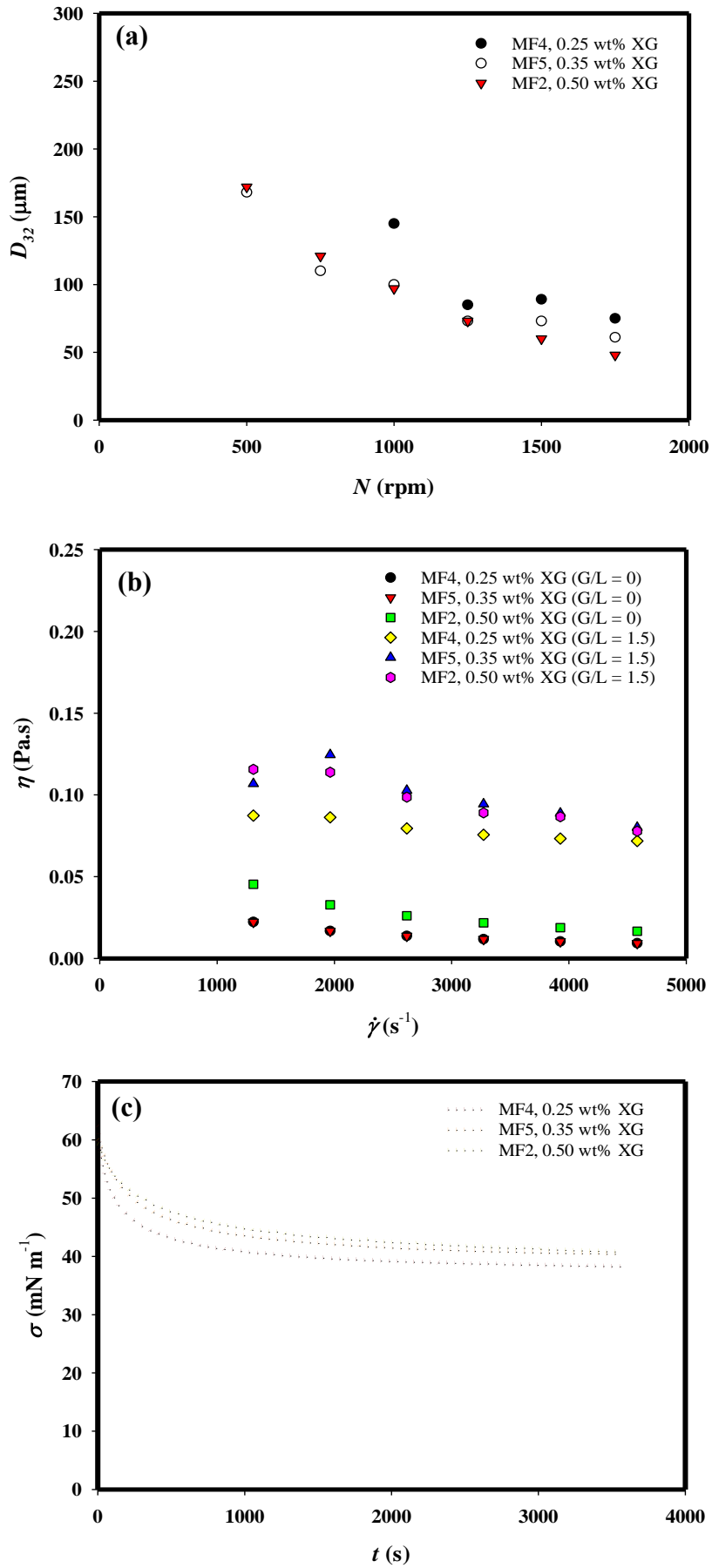


Fig. 11. Effects of Xanthan gum concentration: (a) mean bubble size; (b) dynamic surface tension; (c) apparent dispersion viscosity.

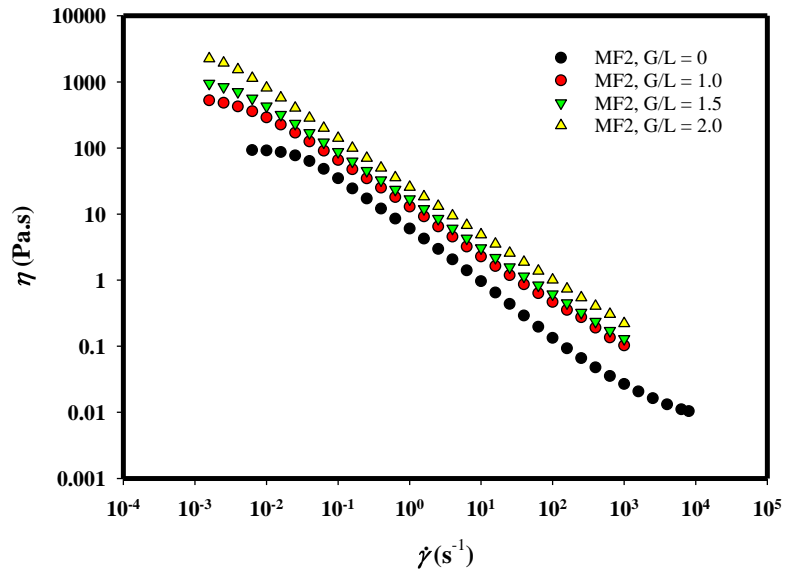


Fig. 12. Typical apparent viscosity curves of fluid MF2 and associated foam generated at $N = 1000$ rpm and different G/L ratios.

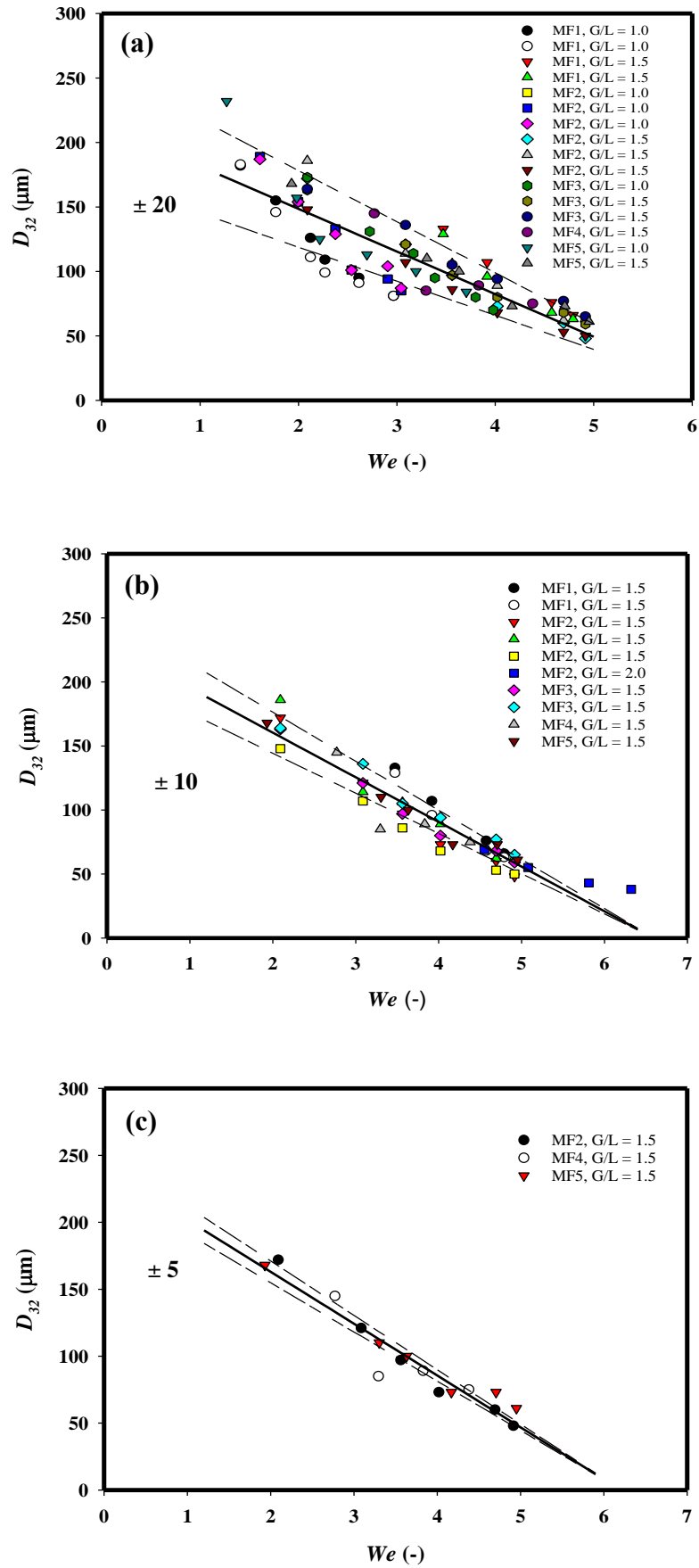


Fig. 13. Variation D_{32} as a function of We for: (a) MF1 – MF5 at $G/L = 1.0 - 2.0$; (b) MF1 – MF5 at $G/L = 1.5, 2.0$; (c) MF2, MF4 and MF5 at $G/L = 1.5$.

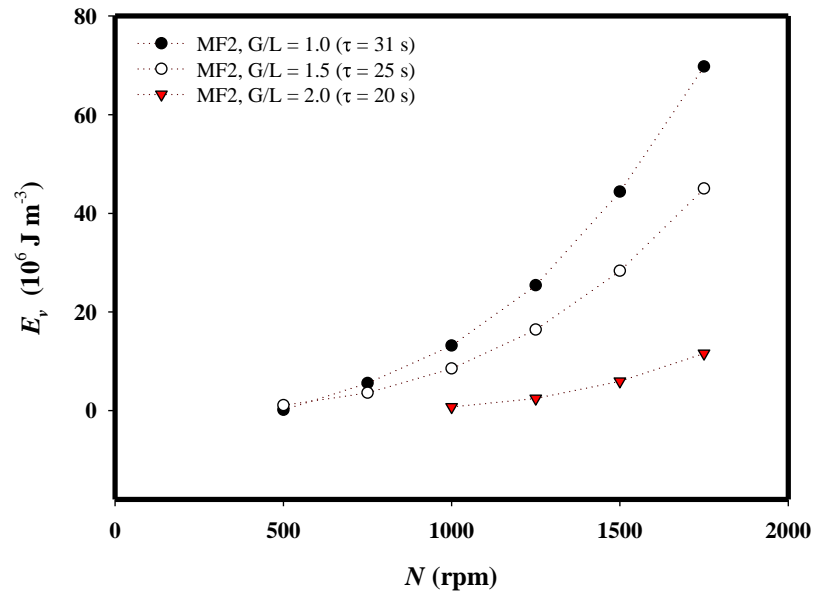


Fig. 14. Effects of rotor speed and G/L ratio on net volumetric energy input

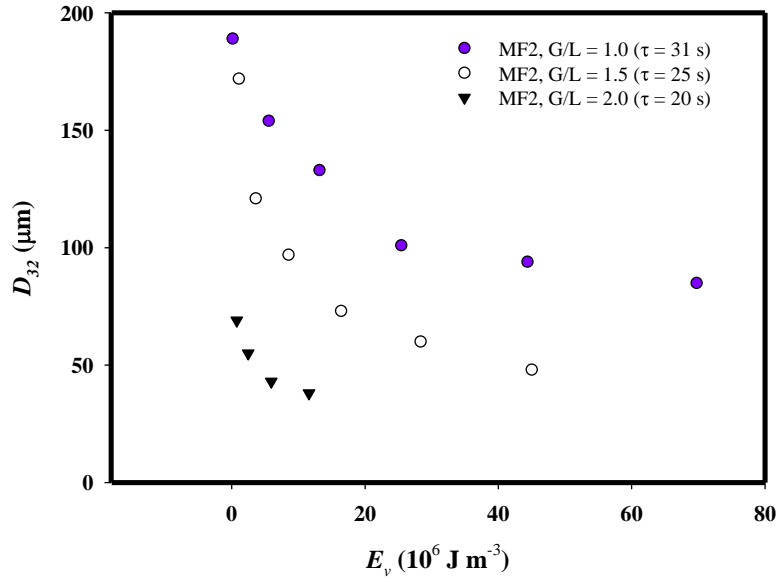


Fig. 15. Variation of D_{32} as a function of E_v .

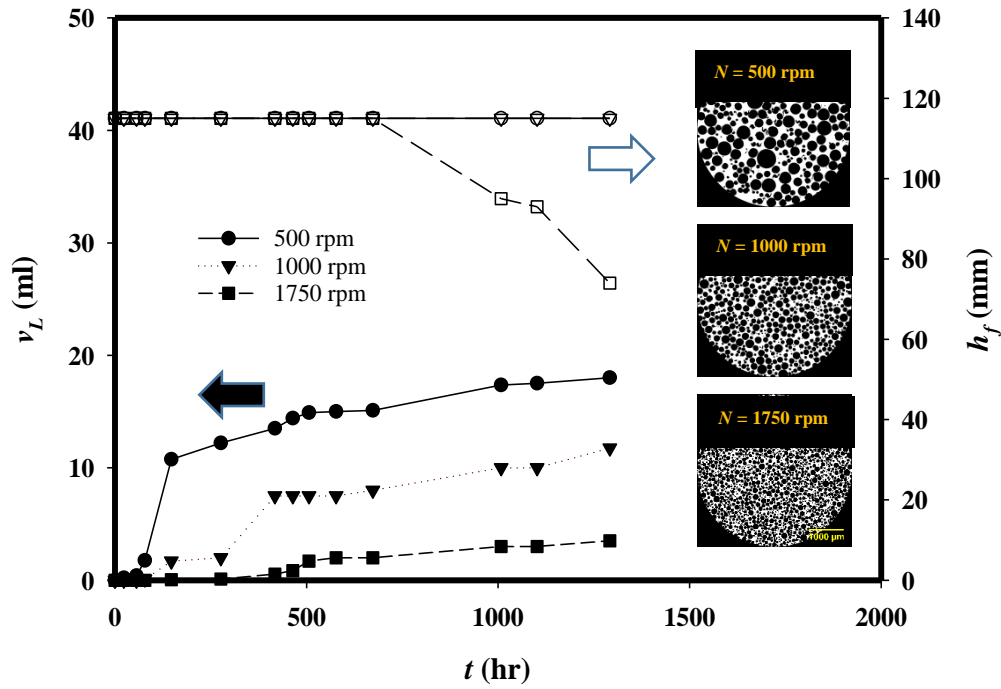


Fig. 16. Typical profiles of foam drainage and collapse for MF2 foams at $G/L = 1.0$ (filled symbols refer to liquid drainage and open symbols refer to foam collapse).

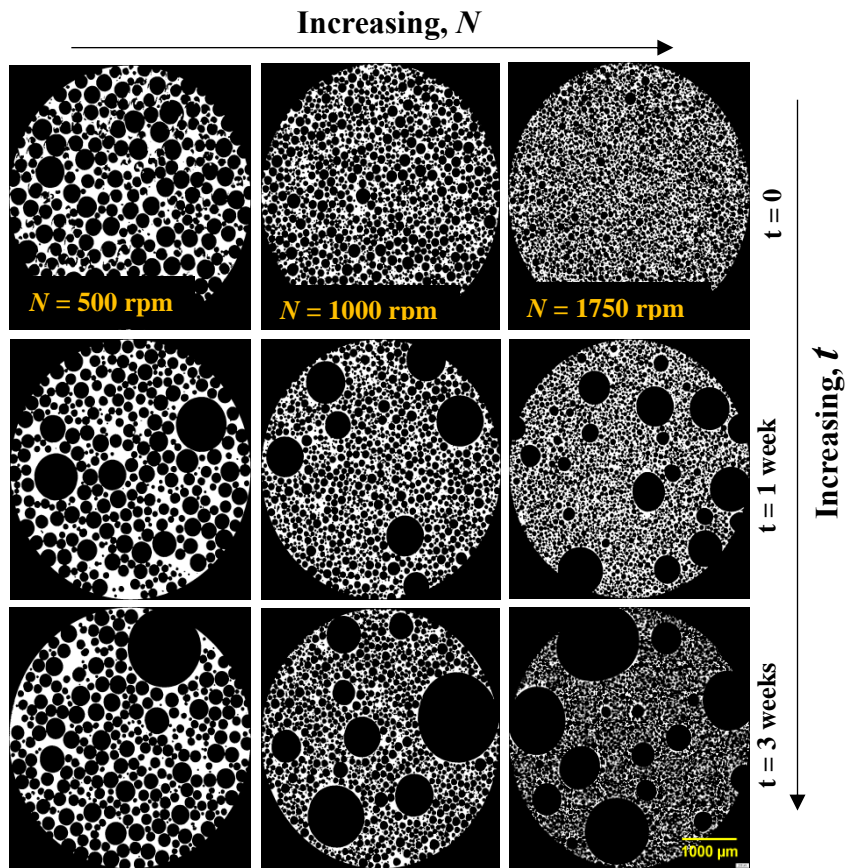


Fig. 17. Typical coarsening X-ray micro-CT images of MF2 foams at $G/L = 1.5$.